STONY BROOK UNIVERSITY

Stony Brook, New York

PICTURING PLASMA: STUDYING THE SIMULATED TRANSVERSE

PROBING OF LASER WAKEFIELD ACCELERATORS

A dissertation submitted in partial fulfillment of the

requirements for the degree of

BACHELOR OF SCIENCE

in

PHYSICS

by

Marisa Elena Petrusky

2021

DEDICATION

To my high school physics teacher, Dr. Liao, who always believed everyone has the

capacity within them to do physics.

ACKNOWLEDGMENTS

ABSTRACT OF THE DISSERTATION

PICTURING PLASMA: STUDYING THE SIMULATED TRANSVERSE

PROBING OF LASER WAKEFIELD ACCELERATORS

by

Marisa Elena Petrusky

Stony Brook University, 2021

Stony Brook, New York

Professor Navid Vafaei-Najafabadi, Research Advisor

With the ability to accelerate charged particles hundreds of times faster than conventional accelerators at a fraction of the size, laser-induced plasma wakefield accelerators (LWFAs) have the potential to revolutionize physics. In a LWFA, a high-powered laser creates a wake of charge within plasma, where particles can be injected and accelerated. To better understand the induced wakefield structure, the Quasi-static Electron Propagation (QuEP) simulation library was developed, as it efficiently sends electron beam probes through pre-generated LWFA electromagnetic fields in three-dimensional space. QuEP allows researchers to quickly generate probe profiles under a variety of beam and plasma conditions, providing a wealth of theoretical insight and giving the researchers at BNL's Accelerator Test Facility (ATF) the computational tools needed to optimize their LWFA experiments.

TABLE OF CONTENTS

CHAPTER 1

INTRODUCTION

1.1 Motivation

Particle accelerators are essential tools for many areas of research, from investigating new physics beyond the Standard Model to producing new medical radioisotopes [1]. In order to continue advancing these fields, accelerators of increasingly higher energies are needed, as the size of the object one wants to observe or interact with is inversely proportional to the energy of its "probe" via the de Broglie equation. Current radio-frequency (RF) technology can accelerate particles with gradients up to 100 MeV/m, with final particle energies reaching the TeV scale given geological, radiation safety, and cost-of-operation constraints [2]. To go beyond this energy frontier, accelerator technology of higher-gradients must be developed.

Plasma-based particle accelerators show great promise in achieving this goal. Ionized gases, or plasmas, can support accelerating gradients on the order of 100 GeV/m. A charged particle bunch or laser pulse driver is sent through the plasma, which results in the highly mobile plasma electrons forming wakefields (or wakes) behind the driver [3]. Understanding the field structure and evolution of these wakes is crucial for advancing plasma wakefield acceleration (PWFA), most notably in ensuring preservation of beam quality during acceleration.

1.1.1 The Laser-Wakefield Acceleration Experiment at ATF

The Accelerator Test Facility (ATF) at Brookhaven National Lab is conducting a series of experiments to study laser-driven plasma wakefield acceleration (LWFA). Using a high-powered CO_2 laser to drive wakes in a plasma cell, an electron beam

is sent transverse to the direction of laser propagation, then observed a certain distance from the cell. This deflected beam profile provides a transverse "snapshot" of the wakefields. Electron beams are ideal for this purpose, as unlike optical probes, charged particles are directly impacted by forces inside a plasma wakefield.

At present, it is cyclically difficult to model the ATF LWFA experiment analytically. Modeling the experiment analytically requires further understanding of the field structure of plasma wakes, but exploring previously unexplored field structures is precisely what this experiment aims to do in the first place. Predictive numerical simulations, on the other hand, have been successfully used in PWFA research for decades. Within this research group in particular, plasma simulation codes were developed to predict relativistic trajectories of charged particles through prescribed cylindrically symmetric electromagnetic fields.

The research described here builds upon said simulations in order to better understand how electron beams are affected by plasma wakefields and how that translates into properties of the plasma wakefields themselves. This thesis aims to demonstrate the methods used to simulate electron beam trajectories, as well as how this simulation tool can be used to gain experimental insights for LWFA experiments.

Chapter 1 introduces the overall motivation behind this research. Chapter 2 provides a brief explanation of laser-driven plasma wakefield acceleration and other scientific terms used throughout this thesis, as well as where this work fits in with ongoing LWFA research. Chapter 3 explains the methods by which this simulation library was developed, including the physics behind single electron motion within a plasma wake, as well as the analytical tests used to verify simulation accuracy. Finally, Chapter 4 details the discoveries made using this library to date, and Chapter 5 summarizes the major accomplishments of this work as well as areas of future study.

2.1 Plasma Accelerator Time Scale and Normalizations

This thesis expresses certain quantities as normalized according to the time and length scales of the plasma. The time scale of a plasma is given by its plasma frequency, ω_p, which is given by

$$\omega_p^2 = \frac{ne^2}{m_e\epsilon_0} \tag{2.1}$$

where n is the particle number density of the plasma, e is the charge of an electron, m_e is the mass of an electron, and ϵ_0 is the permittivity of free space [4]. Lengths are then normalized in units of c/ω_p, where c is the speed of light in a vacuum and time is expressed in units of ω_p^{-1}. Electromagnetic fields are normalized by $mc\omega_p/e$.

2.2 Laser-Driven Plasma Wakefield Accelerators

In a laser-driven plasma wakefield accelerator, a high-power, ultrashort laser pulse is sent through plasma in order to induce the formation of wakefields [5]. As the laser pulse passes through the plasma, it exerts radiation pressure on the charged particles closest to it, causing those particles to be expelled via the ponderomotive force. Due to their lower mass, electrons are the main particles being expelled out into a wake, while the positively charged heavy ions effectively remain in place [6].

If the region behind the driver consists of only ions ($n_e = 0$), the region is said to be fully blown out, and is called a blowout regime. This "bubble" of positive charge travels with the driver at near the speed of light, and remains stable as the pulse propagates. The bubble also contains focusing fields that are linear as a function of
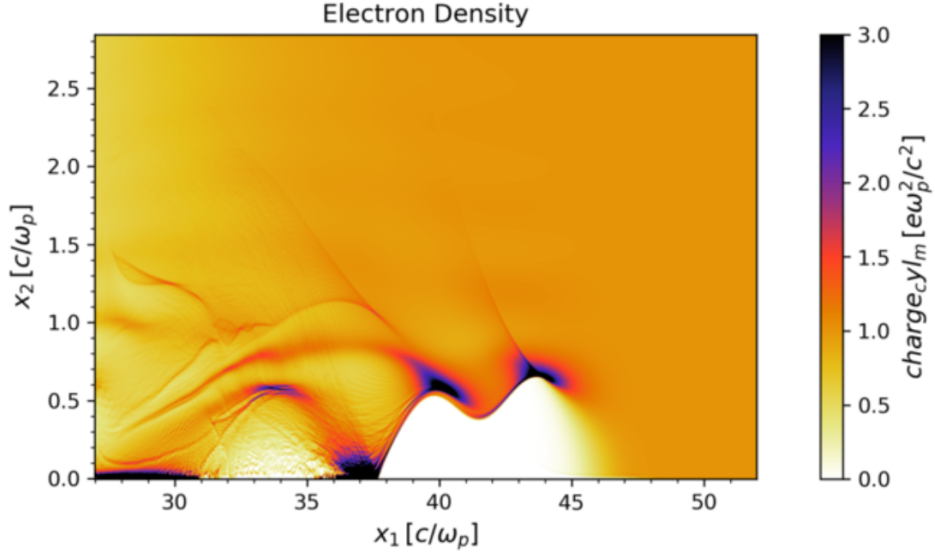
Figure 2.1: Map of electron density for a fully blown out regime. The driving laser propagates along the horizontal axis from left to right, and the vertical axis corresponds to radial distance from the laser pulse's direction of propagation. Magnitude of electron density is shown on the color axis, with white corresponding to complete absence of electrons.

radius. Charged particles (e.g. electrons) injected into this wake at the right phase will travel along with the pulse and extract energy from its fields. They will also remain focused due to the transverse focusing fields of the blowout regime. This is a part of what makes LWFA so viable: whereas typical accelerators require large magnets to focus beams, plasma wakes come with their own focusing mechanisms. Meanwhile, the expelled electrons continue to oscillate around their equilibrium positions, maintaining their blown out shape even after the laser pulse has already left the area.

An example of a simulated blowout regime is shown in Figure 2.1, where the front two bubbles from $x_2 = 37.5$ to $x_2 = 45$ are fully blown out. The region from $x_2 = 30$ to $x_2 = 35$ is only partially blown out, but still retains a bubble shape as its electrons continue to oscillate.

2.3 Present Gap in LWFA Research

While theory and simulation have made significant strides in studying LWFA field structures, direct experimental observations are still challenging because plasma wakes are short-lived ($\sim$ ps lifetime), microscopic in size ($\sim \mu$m), and move at the speed of light. Optical probes can be used to study plasma wakes, however, they depend on observing changes in the plasma's density to cause a phase shift in the probe. For low density plasmas ($\sim 10^{17}$ cm^{-3}), plasma density variations result in very small phase shifts, thus optical methods have not been demonstrated for diagnosing wakes. It is also important to further understand the electric field structure rather than density variations since electromagnetic fields are responsible for acceleration and focusing of injected particles [7].

Relativistic electron bunches of a sufficiently short length ($\sim$ fs) are highly suitable for probing LWFA structures since they interact directly with electromagnetic fields. Success has been demonstrated in mapping longitudinal and transverse field structures of electron-driven plasma wakefields with the driving electron bunches [8]. Transverse field structures will further be studied by sending electron beam probes transverse to LWFA propagation.

At present, deflected electron probe profile results have been obtained from ATF, but how they should be interpreted is an active research question. By developing a quick simulation of this transverse probing process, users can go back and forth between changing initial conditions and observing beam profiles, making note of which conditions produce what profile characteristics. A sufficiently accurate simulation can be directly used to model the ATF experiment, providing an opportunity to efficiently optimize experimental conditions.

CHAPTER 3

METHODS

In order to study the impact of laser-induced plasma wakefields on an electron probe, it was necessary to develop a simulation tool capable of rapidly analyzing electron trajectories inside and outside a plasma cell for any experimental configuration. A previous undergraduate student developed a numerical program which took cylindrically symmetric (i.e. $\partial/\partial\phi = 0$) field maps of existing particle-in-cell simulations and propagated single relativistic electrons through them [9]. I then adapted this software for a fully-3D coordinate system to account for cylindrically asymmetric electron motion inside the plasma wakes, as well as motion outside the plasma cell. The underlying physics, numerical methods, and verification of the updated library (named QuEP for Quasi-static Electron Propagation), is presented in this section.

3.1 Coordinate System

QuEP follows a Cartesian coordinate system. The driving laser propagates in $\hat{z}$, with the variable $\xi = z - ct$ being used to follow the propagation of the plasma wakefields behind the laser, where the laser is traveling at the speed of light c for a time t in the $\hat{z}$ direction. Unless stated otherwise, the electron probe was always initiated to travel in the $\hat{x}$ direction, transverse to the laser. Thus, the deflected electron probe is observed in the $z - y$ plane at some distance x from the center of the plasma cell.

The variable $r = \sqrt{x^2 + y^2}$ may also be used to refer to the radial distance from the laser axis for convenience purposes.
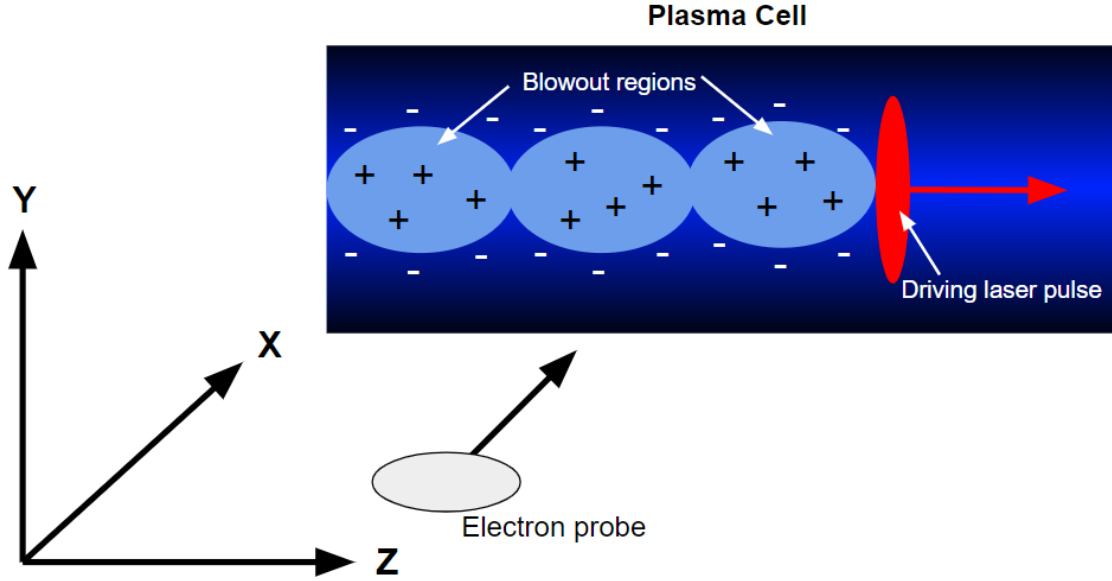
Figure 3.1: Coordinate system of QuEP, with plasma cell and electron probe visuals.

3.2 The Quasi-Static Approximation

In the coordinate system consisting of ξ, the co-moving variable, following the driving laser, the plasma wake changes very gradually from one point to the next inside the plasma. This is known as the quasi-static approximation, and is represented mathematically by

$$\frac{\partial}{\partial z}, \frac{\partial^2}{\partial z^2} \ll \frac{\partial}{\partial \xi} \tag{3.1}$$

With this approximation, one can simulate electron probe trajectories through the plasma without accounting for variation in field structure due to propagation of the wakefields in $\hat{z}$.

3.3 Simulating Single Electron Trajectories

An electron's trajectory is divided into two sections: its motion within the plasma wakefields, and its motion outside the plasma cell until it is observed at a screen.

3.3.1 Motion within the plasma

Every electron is subject to electromagnetic fields in the $\hat{x}, \hat{y}$, and $\hat{z}$ directions according to the Lorentz force $\vec{F}$,

$$\vec{F} = -e(\vec{E} + \vec{v} \times \vec{B}) \tag{3.2}$$

where e is the charge of the electron, $\vec{v}$ is its velocity, $\vec{E}$ is its electric field, and $\vec{B}$ is its magnetic field. For a particle-in-cell simulation, these field values are assigned based on the mesh point the electron currently occupies [10].

From Newton's Second Law, the equations of motion are

$$\vec{F} = \frac{d\vec{p}}{dt} = -e(\vec{E} + \vec{v} \times \vec{B}) \tag{3.3}$$

$$d\vec{p} = -e(\vec{E} + \vec{v} \times \vec{B}) \cdot dt \tag{3.4}$$

If we assume the change in momentum $d\vec{p}$ is constant over a time step dt, then given $\vec{E}$ and $\vec{B}$ at time t, the change in momentum from t to $t + dt$ can be calculated from Equation 3.4. The electron's change in position $d\vec{x}$ can then be calculating by finding the change in velocity $d\vec{v}$ from $d\vec{p}$ and numerically integrating. This is known as a First Order Runge-Kutta method, and its error depends on the order of the time step $\mathcal{O}(t)$ used [11].

To find the proper $d\vec{x}$, consider the relativistic definition of momentum,

$$\vec{p} = \gamma m \vec{v} \tag{3.5}$$

where m is the particle mass and γ is the Lorentz factor given by

$$E^2 = (\gamma mc^2)^2 = p^2 c^2 + (mc^2)^2 \tag{3.6}$$

$$\gamma^2 = \frac{p^2}{(mc)^2} + 1 = \bar{p}^2 + 1 \tag{3.7}$$

where E is the relativistic energy and $\bar{p}$ is the momenta in normalized units. Solving for $\vec{v}$ in Equation 3.5 using Equation 3.7 gives

$$\vec{v} = \frac{\vec{p}}{m\gamma} = \frac{\vec{p}}{m\sqrt{\bar{p}^2 + 1}} \tag{3.8}$$

The change in position is then given by

$$d\vec{x} = \vec{v}dt \tag{3.9}$$

using the value of $\vec{v}$ found in Equation 3.8. This concludes the use of the Runge-Kutta method to track an electron's position and momenta at any point within a simulated plasma cell.

3.3.2 Motion outside the plasma

The area outside the plasma is modelled as a vacuum with no electromagnetic fields present. Thus, electrons exiting the plasma follow a ballistic trajectory using the position and momenta values of the last mesh point they occupied within the bounds of the plasma cell. This trajectory can be modeled as follows,

$$
\begin{pmatrix} y \\ y' \end{pmatrix}_{final} = \begin{pmatrix} 1 & dx \\ 0 & 1 \end{pmatrix} \begin{pmatrix} y \\ y' \end{pmatrix}_{initial}
\tag{3.10}
$$

where y and y' represent the position and angle of the electron, respectively, and dx represents the projected distance from the laser axis.

3.4 Simulating Electron Beam Trajectories

In order to simulate an electron probe profile, QuEP makes use of several approximations.

First, QuEP as a whole is not self-consistent. While the pre-existing field maps are self-consistent with respect to each other, they do not update according to the electron probe's properties and trajectory. The probe electrons themselves are also not self-consistent, as each one propagates through the plasma independently.

Second, the electron probe is "cold", meaning emittance and divergence due to factors such as temperature are not accounted for.

Electron probe profiles are then simulated by sending single electrons one after another, initializing their starting positions based on the desired probe shape. By plotting every electron's position at the same projected distance on a single plot, the deflection of an entire electron beam profile can be observed.

These approximations reduce computational and physical complexity, providing a zero-order understanding of plasma wakefield interactions.

3.5 Verification of Software

Before using QuEP to make predictions on LWFAs, it is necessary to verify its integrity. This was done by ensuring electrons would follow trajectories consistent with analytical calculations based on well-known physics.

3.5.1 Overview of OSIRIS-Quasi3D Field Maps

This work utilizes electromagnetic field maps of laser-induced plasma wakefields generated by the Quasi-3D version of the fully relativistic particle-in-cell code OSIRIS [12]. For laser wakefield acceleration specifically, near azimuthal symmetry allows for fields to be expressed using spherical harmonics in ϕ [13]. For example, a force would be expanded as

$$F(r, z, \phi) = Re\left(\sum_{M=0} F^M(r, z)e^{iM\phi}\right)$$
$$= F^0(r, z) + Re(F^1)cos(\phi) - Im(F^1)sin(\phi) + ... \quad (3.11)$$

where the zeroth harmonic ($M = 0$ or M0) contains the effects of the induced wakefield and the first harmonics ($M = 1$ or M1) contain the laser fields (the remaining terms can be truncated). This provides an interesting way to study LWFA, as the effects of the induced wakefield can be studied separately from those of the laser-driver by selecting the proper harmonic terms. The separation of these field effects was especially critical for software verification.

This thesis work (primarily) focuses on low-density plasma ($n_0 = 1 \times 10^{15}$ cm^{-3}, $\omega_p = 1.77 \times 10^{12}$ Hz), with a 10 μm CO$_2$ laser ($\lambda = 10$ μm $= 0.06$ c/ω_p, $a_0 = 1.414$, spot size 60 μm) as the driver. Simulations have shown wakefield features to be clearest under these conditions, as seen in Figure 3.2.

Region I is fully blown out, whereas Region II is not, hence the difference in field strength. In this snapshot of the plasma wakefields, Region I is experiencing the direct force of the laser, as shown in Figure 3.3 and Figure 3.4. Region II's features result from the plasma being further behind the laser, as discussed in Section 2.1 (see Figure 2.1).
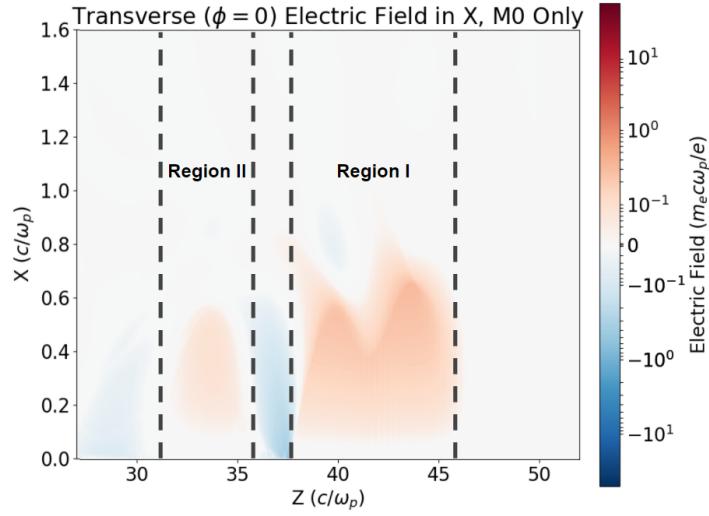
Figure 3.2: Field map of transverse laser-induced electric wakefields, as captured by the zeroth harmonic. Magnitude of the field is shown on the color axis, and the horizontal and vertical axes show longitudinal and transverse position with respect to laser propagation, respectively. The area from $z = 38$ to $z = 46$ will be referred to as Region I, and the area from $z = 32$ to $z = 36$ will be referred to as Region II.

Figure 3.4 shows the total (M0 + M1) transverse electric fields within the plasma cell, and Figure 3.5 shows the total transverse electromagnetic fields. Note that because the laser is polarized in the $\hat{x}$ direction, laser structures are primarily present in E_x and B_y. M0 fields are cylindrically symmetric, hence the presence of an E_y. Traces of laser fields occur in M1 of E_z, which arises as required by the wavefront curvature of a focusing laser pulse.
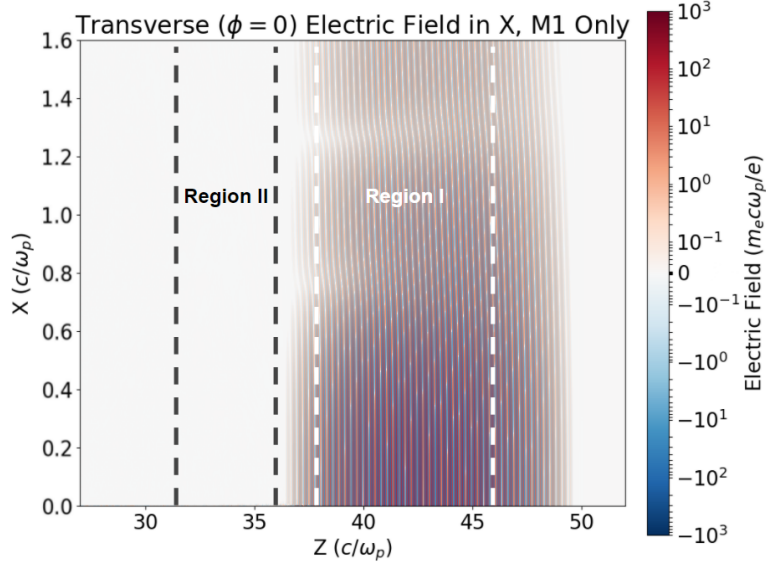
Figure 3.3: Field map of transverse laser electric fields, as captured by the first harmonics. Magnitude of the field is shown on the color axis, and the horizontal and vertical axes show longitudinal and transverse position with respect to laser propagation, respectively.

Figure 3.4: Field map of transverse laser fields superimposed over transverse induced plasma wakefields, as would be seen in a real LWFA. Magnitude of the field is shown on the color axis, and the horizontal and vertical axes show longitudinal and transverse 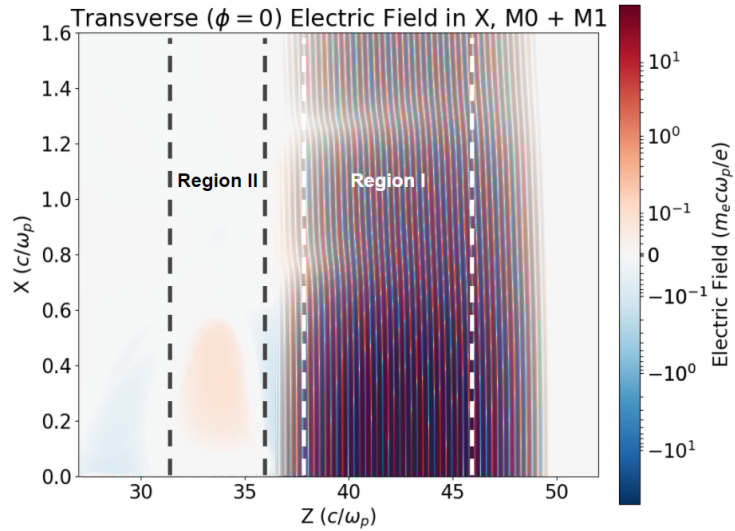position with respect to laser propagation, respectively. Note that the laser fields are saturated here in order to better distinguish M0 structures while keeping a consistent color scale.
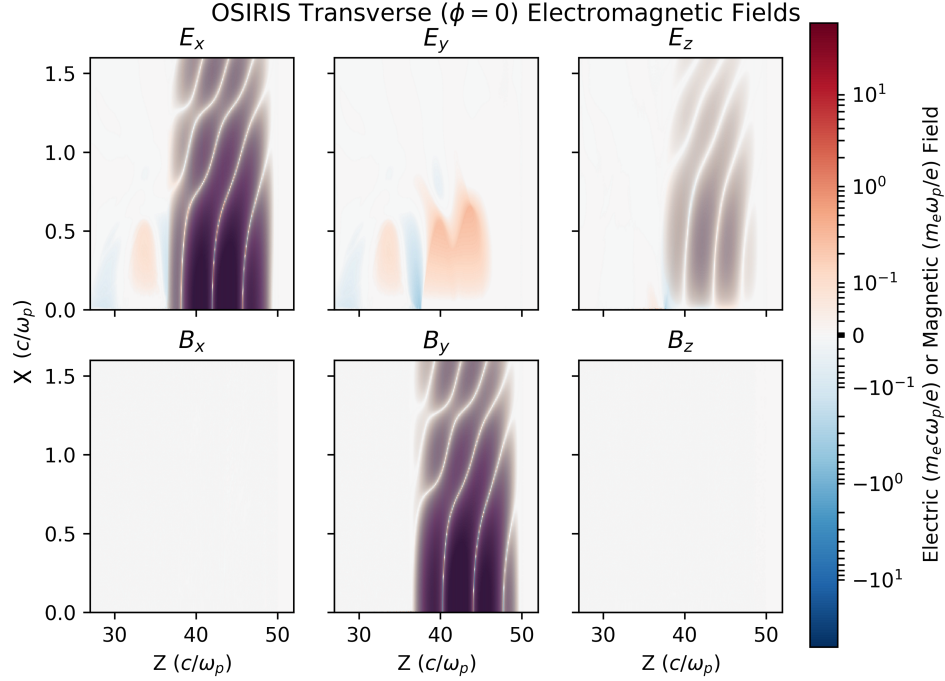
Figure 3.5: Field maps of complete (M0 + M1) transverse electric and magnetic field maps. Magnitude of the field is shown on the color axis, and the horizontal and vertical axes show longitudinal and radial position with respect to laser propagation, respectively.

3.5.2   Observing Betatron Motion

Betatron motion is a type of bounded oscillatory motion that occurs when a charged particle is offset from axis in the presence of a restorative linear field [14]. In PWFAs, restorative fields are formed in blowout regions, making them ideal for electron acceleration as the fields provide a source of focusing. In terms of verifying QuEP, electrons sent within a blowout region should exhibit betatron motion.

Betatron wave number and wavelength in the transverse direction are given by

$$k_\beta = \frac{\omega_p}{c\sqrt{2\gamma}} \tag{3.12}$$

$$\lambda_\beta = \frac{2\pi}{k_\beta} \tag{3.13}$$

Therefore, an electron of $\gamma = 20$ ($p_z = 20$) in plasma of $\omega_p = 1.77 \times 10^{12}$ Hz has a calculated betatron wavelength of $\lambda_{\beta_{calc}} = 39.7 \; c/\omega_p$.

Fully blown out regions are formed from $z = 38$ to $z = 46$. Laser fields are also present in this region, therefore only M0 fields were used to allow for the analysis of electron motion under the force of the focusing wakefields exclusively.

Additionally, the electron was initialized in z such that longitudinal electric field effects were minimized. This is because the betatron wavelength depends on γ, thus any changes in relativistic momentum would impact our test results.
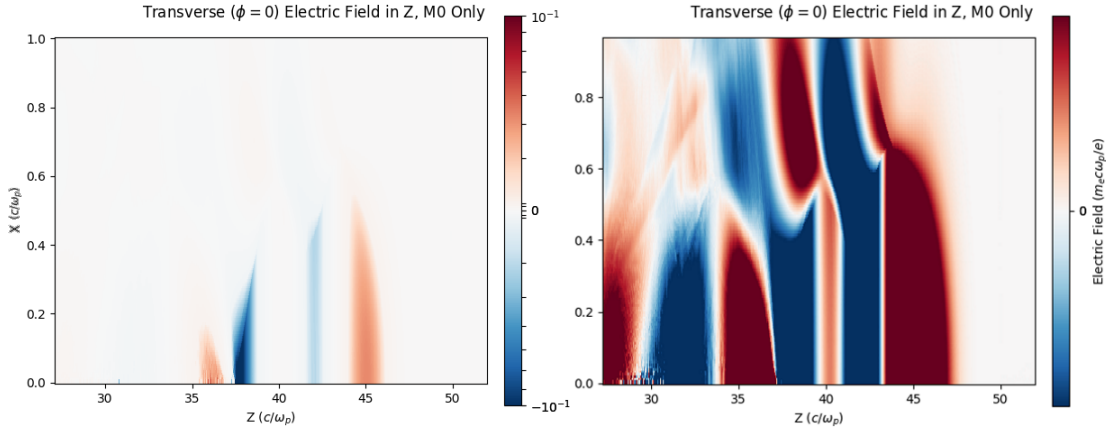
Figure 3.6: M0 electric field in the longitudinal direction. Magnitude of the electric field is shown on the color axis, radial position is shown along the vertical axis, and longitudinal position is shown along the horizontal axis. Left: Unsaturated fields. Right: Saturated fields in order to better distinguish regions with minimal fields, such as $z = 39.7$.

By visual inspection and numerical verification, $z = 39.7$ was determined to be the ideal place to initialize the electron due to its negligible E_z fields, as seen in Figure 3.6. The simulated betatron wavelength was measured to be $\lambda_{\beta_{sim}} = 40.0$

c/ω_p, which has excellent agreement with the calculated $\lambda_{\beta_{calc}} = 39.7\ c/\omega_p$. Thus we conclude that within the plasma cell, QuEP electron propagation is consistent with analytical calculations.
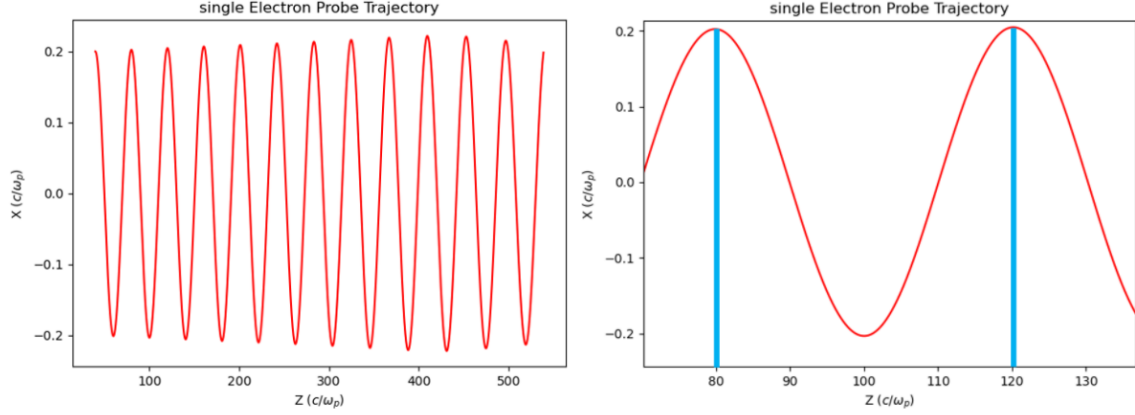

Figure 3.7: Trajectory for an electron initialized at $(x_0, y_0, z_0, p_z) = (0.2, 0.0, 39.7, 20)$. Left: Complete electron trajectory. Right: The betatron wavelength was measured $\lambda_\beta = 40.0\ c/\omega_p$. Lines are superimposed as visual guides.

3.5.3   Testing the Thin Lens Approximation

The linear focusing fields of blowout regions allow for a thin lens approximation analysis. A converging thin lens will see rays sent perpendicular to the lens at distance y_0 from the axis bend towards said axis at angle θ with the vertical upon exiting the lens (see Figure 3.8). They then intersect the axis at the focal point f. For an electron, θ is defined by

$$tan(\theta) = \frac{p_x}{p_y} \tag{3.14}$$

which, after applying the small angle approximation, gives a focal length of

$$f = tan(\theta)y_0 = \theta y_0 = \frac{p_x}{p_y}y_0 \tag{3.15}$$
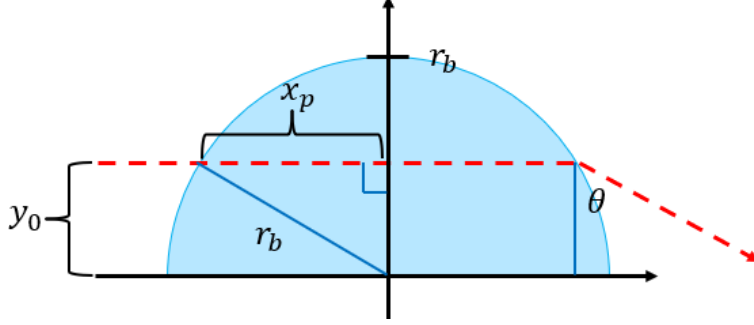
16

Figure 3.8: Diagram of the variables used in the thin lens approximation test. The vertical and horizontal axes display y and x position, respectively.

If $p_{y0} = 0$, p_y is equal to the change in y-momentum Δp_y through the blowout region, which is defined as

$$\Delta p_y = \int_{t_0}^{t} F_y dt' \tag{3.16}$$

where F_y is the y-component of the force integrated over the time spent in the region. The change in x-momentum is small ($\Delta p_x / p_x \ll 1$), so we assume p_x and v_x are constant. This means the time spent in the region is defined as

$$\Delta t = \frac{2x_p}{v_x} \tag{3.17}$$

where x_p is half the horizontal distance spent in the bubble, given by $x_p = \sqrt{r_b^2 - y_0^2}$, where r_b is the radius of the blowout bubble.

The radial force is given by $F_r = kr$, where k is the linear slope of the electric force. F_y is then given by

$$F_y = F_r cos(\theta) = kr cos(\theta)$$
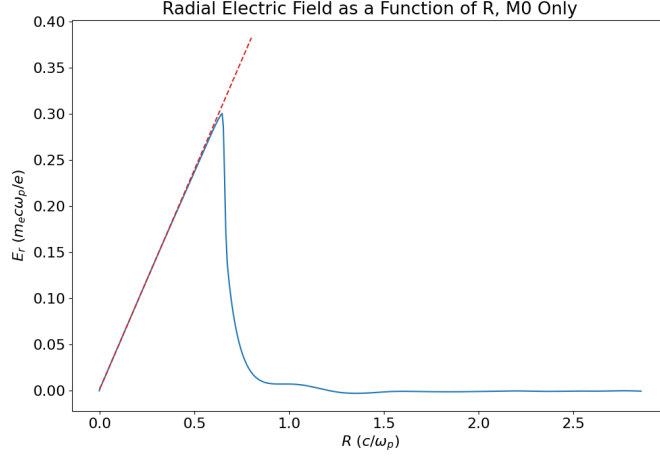$$= k \left(\frac{y_0}{cos(\theta)} \right) cos(\theta)$$
$$= ky_0 \tag{3.18}$$

17

Figure 3.9: M0 electric fields within blowout region at $z = 43.7$. Radial position is shown along the horizontal axis (M0 fields are symmetric in r), while the vertical axis corresponds to a curve showing magnitude of the radial electric field. The restorative linear relationship is clearly observed from $r = 0$ to $r = 0.65$, where $E_r = (0.475 \pm 0.000643)r$. The linear fit is plotted in red.

k is constant for an electron moving at relativistic speeds in the longitudinal direction [15], which would make F_y constant. Thus, the integral of F_y over time becomes $F_y \Delta t$. Returning to Equation 3.15, one can calculate the focal length of a blowout bubble as

$$
\begin{aligned}
f &= \frac{p_x}{p_y} y_0 = \frac{p_x}{\int_{t_0}^t F_y dt'} y_0 \\
&= \frac{p_x}{F_y \Delta t} y_0 = \frac{p_x}{k y_0} \cdot \frac{v_x}{2 x_p} \cdot y_0 \\
&= \frac{p_x v_x}{2 x_p k}
\end{aligned}
\tag{3.19}
$$

This result is particularly significant for experimental purposes because the focal length can be re-written as a function of the maximum transverse focusing force, $F_{\perp_{max}}$. Given $F_{\perp_{max}} = k r_b$, $p_x \approx p$, and re-writing $v_x = p_x/\gamma m = p/\gamma m$, $x_p = \sqrt{r_b^2 - y_0^2} = r_b \sqrt{1 - (y_0/r_b)^2}$, Equation 3.19 gives

$$f = \frac{p_x v_x}{2x_p k} = \frac{p}{2k} \cdot \frac{1}{r_b \sqrt{1 - (y_0/r_b)^2}} \cdot \frac{p}{\gamma m}$$

$$= \frac{p^2}{2\gamma m \cdot k r_b \cdot \sqrt{1 - (y_0/r_b)^2}}$$

$$= \frac{p^2}{2\gamma m F_{\perp_{max}}} \cdot \left(1 - \left(\frac{y_0}{r_b}\right)^2\right)^{-1/2} \tag{3.20}$$

where the $(y_0/r_b)^2$ term accounts for spherical abberation (the whole term in parenthesis can be considered as "depth of field"). If $y_0/r_b \ll 1$, the depth of field term can be dropped, and the effective focal length becomes the same for all electrons regardless of height. $F_{\perp_{max}}$ can then be written as

$$F_{\perp_{max}} = \frac{p^2}{2\gamma m f} \tag{3.21}$$

which is the equation for a thin lens approximation. Within Equation 3.21, only f must be experimentally measured; the other terms are given by the electron probe initialization. Therefore, if the size of one's beam can be made very small, much information can be extracted, including the density of the wake.

To find the analytically calculated focal length, I took one specific case of an electron trajectory where $y_0 = 0.25$, $p_x = 110$, $p_z = 1000$, and $v_x = 0.1$ (in normalized units). $p_z = 1000$ allows the electron to keep up with the wakefield moving at the speed of light, and also allows us to make the approximation that k and F_y are constant. Fitting the linear portion of the curve shown in Figure 3.9, we have $k = 0.475 \pm 0.000643$, as well as $r_b = 0.65$ for an electron sent at $z = 43.7$, all in normalized units. This gives $x_p = 0.6$. From Equation 3.19, the expected focal length is $f_{calc} = 19.30 \pm 0.26 \ c/\omega_p$.

I then sent an electron with these initial parameters through QuEP with only M0 fields (laser effects are not required here), then plotted the appropriate variables

against x-position. Simulated values were determined by taking F_y and p_y from Figure 3.10 once the electron left the plasma ($x \approx 2.5$), calculating f from F_y and p_y, then re-confirming f graphically by noting where the electron trajectory crosses the y-axis (see Figure 3.11). Excellent agreement was found between the calculated and simulated values, as seen in Table 3.1, with a simulated focal length $f_{sim} = 19.64$ and an absolute error of 0.34 c/ω_p with f_{calc}. Thus we conclude that QuEP electron propagation is consistent with analytical calculations.

Table 3.1: Comparison between expected and simulated focal length values.

	Expected	Simulated
$F_y = ky_0$	0.12	0.12
$p_y = F_y\Delta t$	1.40	1.40
f	19.30	19.64
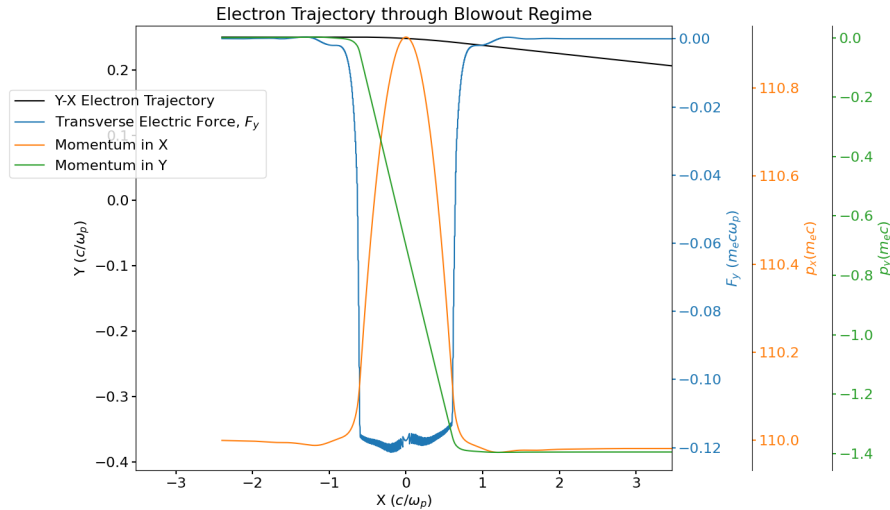
Figure 3.10: Single electron trajectory through plasma keeping up with the wake. The horizontal axis shows x-position, while the vertical axes correspond to curves showing y-position (black), transverse force F_y (blue), p_x (orange), and p_y (green), all in normalized units.

Figure 3.11: Graphical confirmation of simulated focal length $f_{sim} = 19.64\ c/\omega_p$. The vertical and horizontal axes show y-position and x-position, respectively. Lines are superimposed as visual guides.

CHAPTER 4

RESULTS

Upon verifying that its electron propagation methods are consistent with known physics, QuEP can reliably be used as a computational tool for predicting the impact of a laser-induced plasma wakefield on an electron probe. The predictions made using QuEP to date a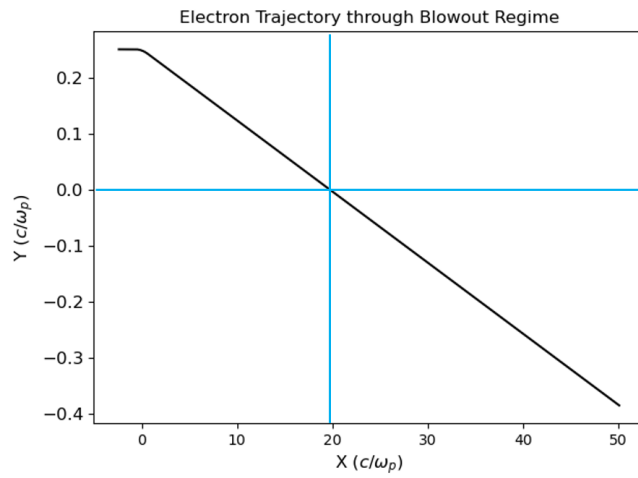re described in the following section, including a qualitative comparison with experimental results obtained from ATF, how the laser and induced wakefield affect the electron probe profile, how probe profile changes with varying transverse height, and how experimental focal lengths differ from theoretical expectations.

4.1   Qualitative Comparison with Experimental Results

There is strong qualitative agreement between the electron probe simulated by QuEP and the experimental results obtained by the Accelerator Test Facility (ATF) at Brookhaven National Lab in Fall 2019, indicating that to a zero-order, QuEP captures the most dominant interactions of electron probes with plasma wakefield structures.

Three distinct characteristics were noted of the deflected electron probe profile during the ATF experiment, as seen in Figure 4.1. First, four nodes (referring to the three bright spots and a point along the left side of the structure between the green dashed lines) were formed, with electrons in between forming a bubble-like structure. Second, streaks of electrons formed around the nodes and bubbles. Blue dashed lines are shown parallel to, but not overlapping, these streaks in Figure 4.1. Finally, a "mast and sail" of electrons formed on the side of the electron probe closest to the laser pulse, and is shown between the green dashed lines. The mast refers to the vertical line of electrons to the right of the leftmost green line, and the sail
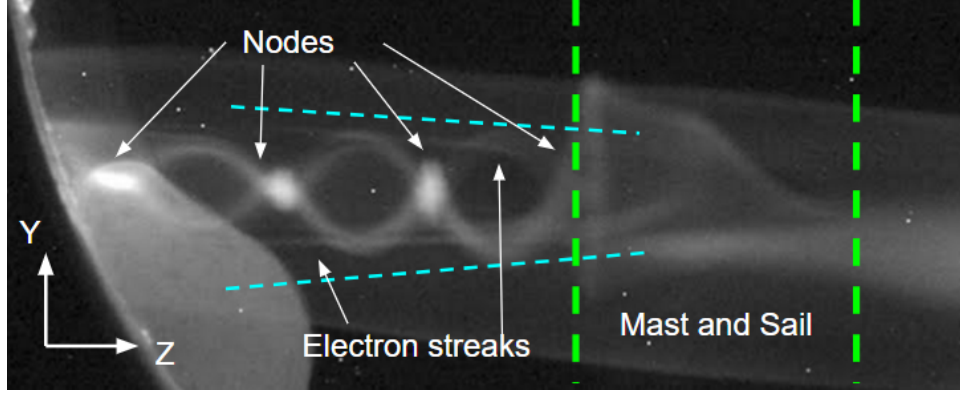
Figure 4.1: Photo of deflected electron probe profile 500 mm from plasma cell. The vertical and horizontal axes point in the y and z-position, respectively. Brightness corresponds to electron density. Lines are superimposed as visual guides for key features.

refers to the sloped shape to the right of it, ending in a point on axis. Although experimental conditions are not precisely known in these preliminary experiments, based on feature sizes it was estimated that the density was 1×10^{15} cm^3. Quasi-3D OSIRIS simulations predict that the ATF laser pulse at this density creates field structures that was shown in Chapter 3. We therefore examined the structures made by low and high density electron probes as a qualitative comparison of simulation results with experiments.

To parallel the conditions of the ATF experiment, a rectangular electron probe of $(p_x, p_y, p_z) = (110, 0, 0)$ and widths $(w_y, w_z) = (1.0, 24.0)$ $[c/\omega_p]$ was sent such that the probe passed through the plasma cell from $z = 27$ to $z = 51$ (see Figure 3.2). Both M0 and M1 fields were used. The electron probe was then observed at a distance of 500 mm from the plasma cell.

During the ATF experiment, the electron probe had a "step" density profile such that the beam had a very dense core with less dense "wings". In QuEP, each rectangular electron probe has a uniform density profile. Two beam densities were studied: a high density, where electrons were spaced $\lambda/60 = 0.001$ c/ω_p apart, and a
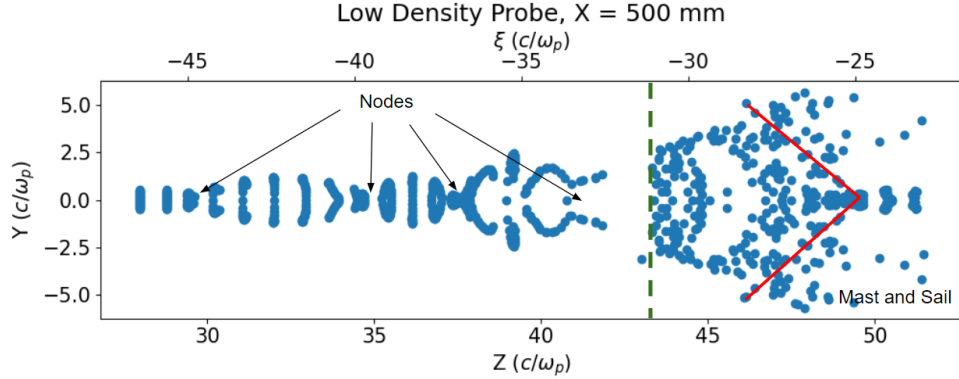
Figure 4.2: Simulation of deflected low density electron probe profile 500 mm from plasma cell. The vertical and horizontal axes correspond to y and z-position, respectively. Each dot represents the position of a single electron (not to scale). Lines are superimposed as visual guides for key features.

low density, where electrons were spaced 0.5 c/ω_p apart. These two configurations are called "high density" and "low density" probe profiles in the remainder of this thesis. The high density profile allows field interactions much smaller than the laser wavelength to be observed, while the low density profile makes it easier to study the overall shape of the deflected probe.

Within the low density profile (as seen in Figure 4.2), the four nodes are observed at $z \approx 30, 35, 38.5$ and 41. There are also three bubbles, with the left-most bubble having an elongated shape compared to the previous two. A mast is observed around $z \approx 44$ (marked by the green dashed line), with a vaguely triangle-like sail formed in front of it (outlined in red).

It is worth noting that shifting low-density probes leads to drastically different profile shapes at the front of the probe. This re-iterates the importance of comparing low-density data to high-density data, as high density probe profile features are far more definitive and visually pronounced.

Within the high density profile (as seen in Figure 4.3), the four nodes are observed at $z \approx 30, 34.5, 37.5$ and 42. Two lines of charge are observed, one at $z = 42$ and
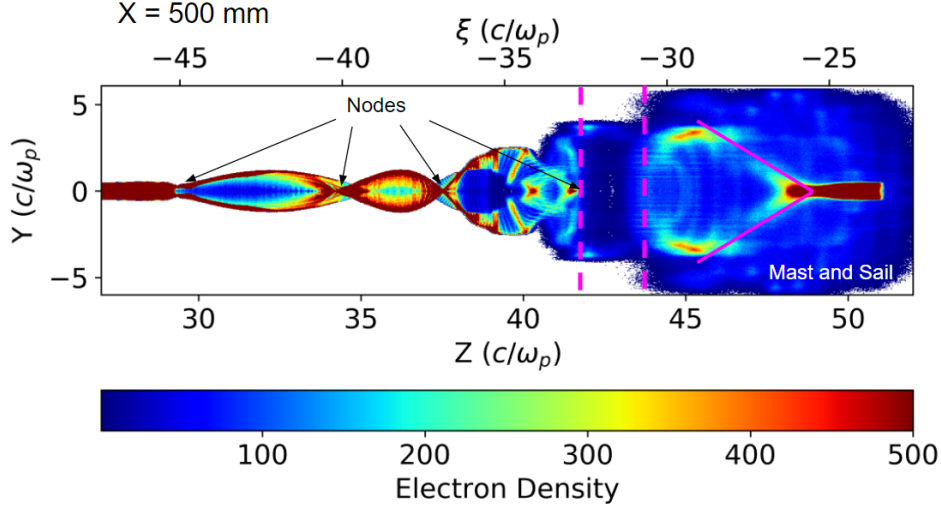
Figure 4.3: Simulation of deflected high density electron probe profile 500 mm from plasma cell. Electron density is shown on the color axis with a bin size of 0.03 c/ω_p ($\lambda/2$), while the vertical and horizontal axes correspond to y and z-position, respectively. Note that only bins with an electron count greater than 5 are given color values, and that the color values are saturated for clarity of features.

the other at $z = 44$ (marked by the pink dashed lines). While only one mast is seen in the ATF experiment photo, two masts are expected based on the fact that there are two blowout bubbles within Region I (see Figure 3.2), each of which contains restorative electric fields in z that push electrons towards the center of the bubble (see Figure 3.6). The sail shape is marked by the solid pink lines.

While the high density profile's bubble-structures in Region II are just as pronounced as the low density profile and the ATF experiment photo, the features at the front of the probe rest inside a large electron cloud. There is also a block of electrons in front of the probe (the red rectangular shape from $z = 48$ to $z = 51$), which results from part of the probe passing through the area ahead of Region I where the fields are significantly weaker.

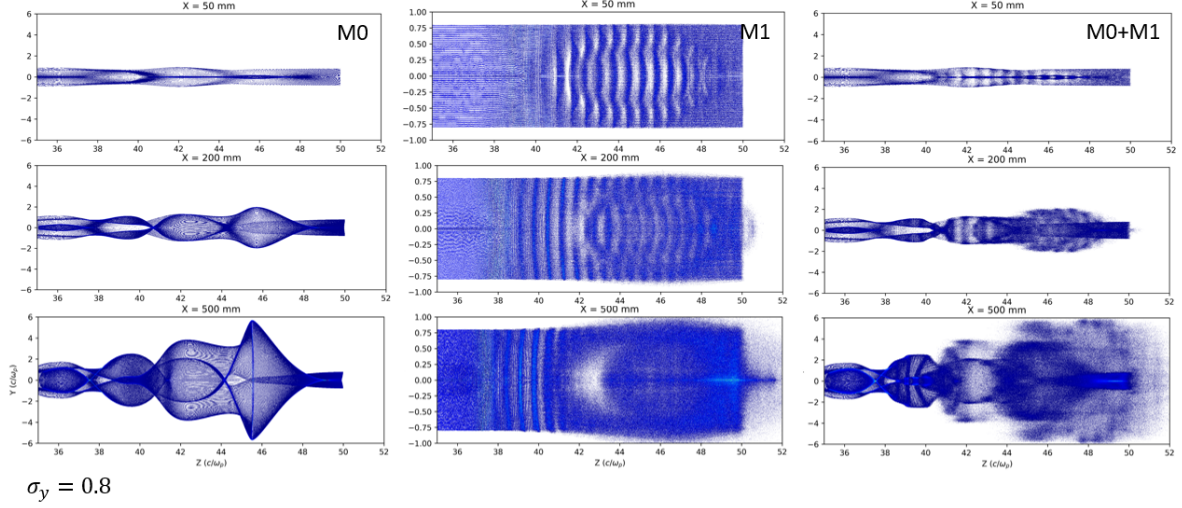## 4.2 Impact of Laser versus Induced Wakefield

$\sigma_y = 0.8$

Figure 4.4: Electron probe of $(w_y, w_z) = (1.6, 15.0)$ sent through only M0, only M1, and M0+M1 fields, respectively. Electron density is shown on the color axis with a bin size of 0.006 c/ω_p ($\lambda/10$), while the vertical and horizontal axes correspond to y and z-position, respectively. Note the change in axes limits for the M1 (middle) plot, and that only bins with an electron count greater than 5 are given color values.

The OSIRIS-Quasi3D software's separation of field effects into azimuthal harmonics prompted the study of the electron probe under one mode at a time. By comparing these profiles to the profile of the electron probe under full field effects, characteristics of the M0+M1 electron probe can be attributed to either the laser or the induced wakefield.

A probe was sent with $(p_x, p_y, p_z) = (110, 0, 0)$ and $(w_y, w_z) = (1.6, 15.0)$ $[c/\omega_p]$ was sent such that the probe passed through the plasma cell from $z = 35$ to $z = 50$, then projected to various distances up to 500 mm. Select plots from this study are shown in Figure 4.4.

This study indicated the induced wakefields (M0) dominate the overall shape of the probe. The transverse fields cause electrons to focus and defocus, resulting in the overall bubble-like structure observed in both the M0 and M0+M1 plots (see

leftmost column of Figure 4.4). The "masts and sail" features also originate from the induced wakefields, as at $x = 500$ mm, a mast can be observed at $z = 45.5$ with a symmetric sail shape in front of it, and the second mast trailing behind it at $z = 41.5$.

Under the laser fields exclusively (see middle column of Figure 4.4), modulation features appear in $\hat{z}$, which results in the blurring of probe features close to the laser pulse as the probe moves in x. Very little motion occurs in the transverse direction, as the probe remains roughly the same size in y throughout its trajectory. Two different types of modulation are observed. Fine modulation structures, best observed at $x = 500$ mm from $z = 37$ to $z = 38$ in Figure 4.5, are spaced the laser wavelength λ apart. These features are expected, as lasers directly create oscillations in electromagnetic fields of their own wavelength apart in plasma, where positive and negative charges can move freely. The larger modulation structures, noticeable in all three M1 plots featured in Figure 4.4 as well as from $z = 38.5$ to $z = 40$ in Figure 4.5, are spaced 10λ apart. These larger modulations overlap with the region of highest laser intensity, whereas the fine modulations overlap with the region of gradually weakening laser fields. Therefore, since the fine modulations were expected but the large ones were not, it is likely that the fine modulations form throughout the probe profile, but are overshadowed in the region of high laser intensity by the additional formation of the large modulation structures. Aside from this prediction, the origin of the large modulation structures, especially their spacing of 10λ, is an area of active study.

With respect to electron probes sent through M0+M1 fields, laser modulation clearly disrupts the smoothness of the probe profile produced by the induced wakefields. Comparing the M0 and M0+M1 probes in Figure 4.4 at $x = 50$ mm (top row), the difference between the profiles is the modulation stripes from $z = 40$ to
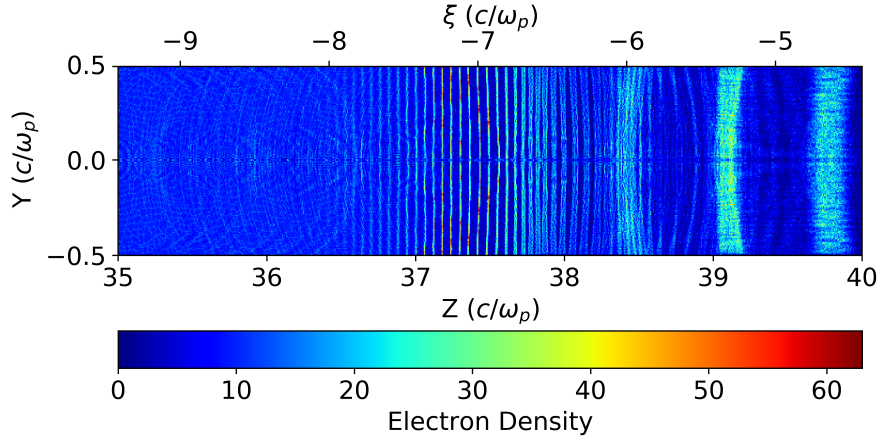
Figure 4.5: Electron probe of $w_y = 1.0$ sent through only M1 fields, viewing only the deflected probe from $z = 35$ to $z = 40$. Electron density is shown on the color axis with a bin size of 0.006 c/ω_p ($\lambda/10$), while the vertical and horizontal axes correspond to y and z-position, respectively.

$z = 48$. At 200 mm, the movement of electrons in z and y due to the additional field of the laser cause fine structures in the bubble between $z = 44$ and $z = 48$ to wash out. By 500 mm, the majority of the features at the front of the probe wash out, including the rightmost mast. Fine and large modulation features can also be seen in the M0+M1 bubble located from $z = 38$ to $z = 40$.

4.3 Varying Probe Height

A study of vertical probe height (w_y) variation provided insight into how probe profile features change with initial probe size. Probes of $(p_x, p_y, p_z) = (110, 0, 0)$, $w_y = 0.5, 1.0$, and 1.6, and $w_z = 24.0$ were sent through (independently) such that the probes passed through the plasma cell from $z = 27$ to $z = 51$. $w_y = 0.5$ was chosen to observe field effects when the probe remained close to axis, while $w_y = 1.6$ was chosen to observe field effects when the probe had a height corresponding to the maximum radius of the blowout bubbles (see Figure 3.2). $w_y = 1.0$ was used as the
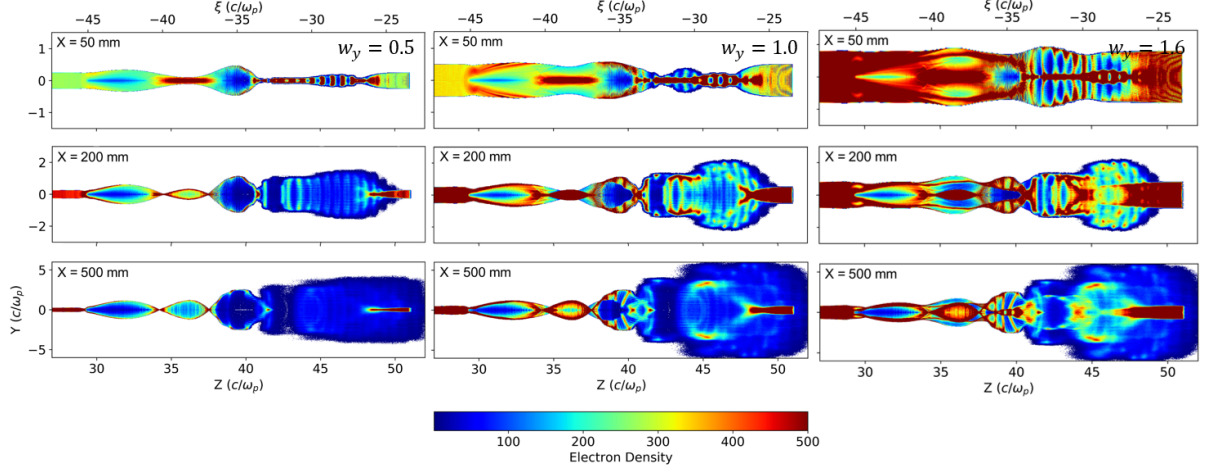
Figure 4.6: Electron probe of $w_y = 0.5, 1.0$, and 1.6 and $w_z = 24.0$ sent through M0+M1 fields, respectively. Electron density is shown on the color axis with a bin size of $0.006\ c/\omega_p\ (\lambda/10)$, while the vertical and horizontal axes correspond to y and $z-$position, respectively. Note that only bins with an electron count greater than 5 are given color values, and that the color values are saturated for clarity of features.

intermediate probe profile, which was used in the previous section to compare with experimental results. Both M0 and M1 fields were used.

Figure 4.6 compares the probe profile at various distances up to 500 mm. $w_y = 0.5$ (leftmost column) makes the two masts at $z = 42$ and $z = 44$ very prominent since the profile is comparatively empty between them (see area between pink dashed lines in Figure 4.7). This indicates the area between the masts is filled by electrons initialized further from axis, as the probes of $w_y = 1.0$ (middle column) and $w_y = 1.6$ (rightmost column) show this area as increasingly populated with increasing probe height. With the $w_y = 0.5$ probe, the four nodes and bubble structures are still visible, indicating these structures form at even the shortest of probe heights due to the impact of the transverse force as expected of Equation 3.20. In fact, the nodes at $z = 34.5$ and $z = 37.5$ are not surrounded by electrons above and below them; they appear point-like against the background, compared to the other two profiles, which have electrons forming round structures around the nodes.

$w_y = 1.6$ reveals a variety of interesting (but experimentally distracting) features forming from probes with electrons initialized further from axis. These features primarily result from electrons further from axis focusing much farther than electrons close to axis (see Chapter 3). Surrounding the back bubble-structures is a "layer" of electrons, which broadens the shape of the back bubbles. The bubble from $z = 37.5$ to $z = 42$ contains a dense center ($y = 0$) which appears martially modulated by the laser. Figure 4.8 points out both features. These features are "experimentally distracting" because they obscure the bubble-structures in Region II. The back bubbles are the most well understood features in the study of transverse electron probes through LWFA. Their lensing can more easily be tracked in order to measure focal length, which directly leads to calculation of plasma density (see Chapter 3). Thus, the back bubbles need the most visual clarity in real experiments.

As a result, this study predicts that smaller w_y are better for future LWFA transverse electron probing experiments. Though the minimum possible beam size is limited by the electron beam optics, one potential way to shorten the beam height after it is generated is to place a slotted mask in front of the beam.
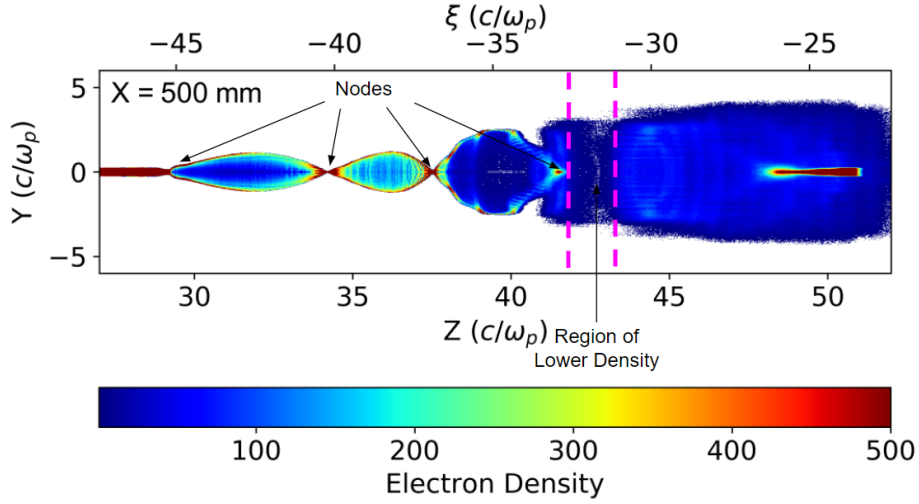
Figure 4.7: Electron probe of $w_y = 0.5$ sent through M0+M1 fields, projected to $x = 500$ mm. Electron density is shown on the color axis with a bin size of 0.03 c/ω_p ($\lambda/2$), while the vertical and horizontal axes correspond to y and z-position, respectively. Note that only bins with an electron count greater than 5 are given color values, and that the color values are saturated for clarity of features.

Figure 4.8: Electron probe of $w_y = 1.6$ sent through M0+M1 fields, projected to $x = 500$ mm. Electron density is shown on the color axis with a bin size of 0.03 c/ω_p ($\lambda/2$), while the vertical and horizontal axes correspond to y and z-position, respectively. Note that only bins with an electron count greater than 5 are given color values, and that the color values are saturated for clarity of features.
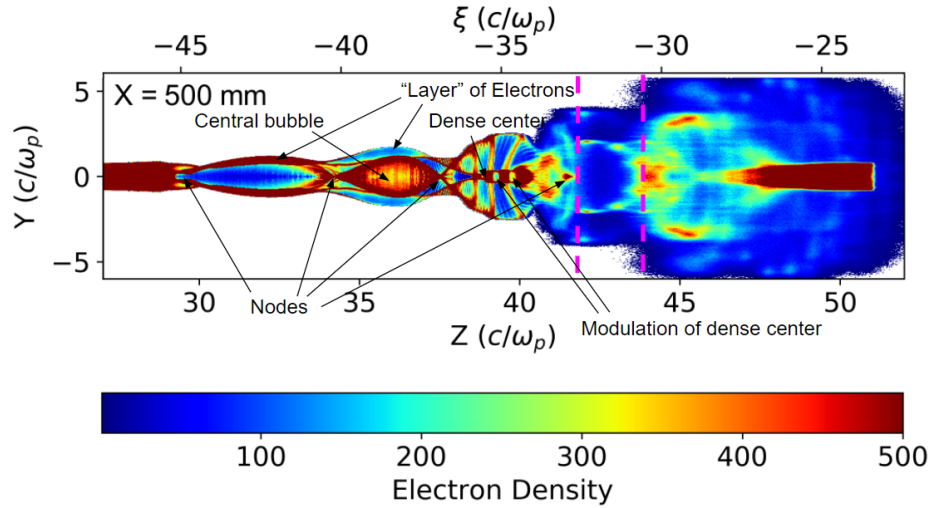
4.4 Experimental Focal Lengths and Transverse Size of Probe

It is useful to examine the "experimental" focal lengths of electrons for deciding what distance to project the electron probe to, as well as the focal length variation with transverse size. To do so, p_z is set to 0, as it would be during an experiment, since electron probes will be sent exactly transverse to the plasma wakefield and thus will not keep with the co-moving plane. The (x_0, ξ_0) values were also set to (-2.4, -5.9) such that the electron beam will pass through $z = 43.7$, the center of the front-most bubble, at $x = 0$. This allows us to use the measured k value from Figure 3.9 in our calculations. Additionally, for y_0/r_b not $\ll 1$, a single uniform focal length is limited by spherical abberation, as seen in Equation 3.20 (the relevant parts of equations used in this analysis are reproduced below). We attempt to better understand this effect in the following.

$$f = \frac{p_x}{p_y} y_0 \tag{3.15}$$

$$f = \frac{p_x v_x}{2 x_p k} \tag{3.19}$$

$$f = \frac{p^2}{2\gamma m F_{\perp max}} \cdot \left(1 - \left(\frac{y_0}{r_b}\right)^2\right)^{-1/2} \tag{3.20}$$

First, the focal length was calculated for electrons with values of y_0/r_b between 0 and 0.65 using Equation 3.19. For $p_z = 0$, note that $v_x = 1$, and from Figure 3.9, $k = 0.475$ and $r_b = 0.65$ at $z = 43.7$. Depth of field was also calculated using the y_0/r_b dependent term from Equation 3.20, and is used for the "error" in theoretical focal length. Then, electrons of the same y_0/r_b were sent through QuEP, and focal length was measured and verified using Equation 3.15. The QuEP focal lengths are
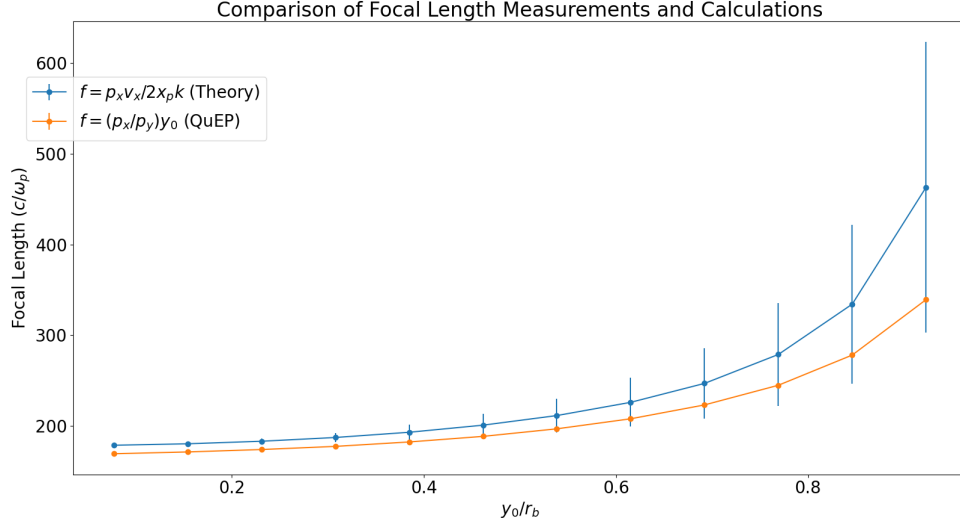
Figure 4.9: Focal lengths of single electrons for various values of y_0/r_b. The blue points represent focal lengths calculated with Equation 3.19, with error bars corresponding to depth of field (see Equation 3.20). The orange points represent focal lengths found through QuEP, with each electron initialized with $(x_0, \xi_0) = (-2.4, -5.9)$. The vertical and horizontal axes correspond to focal length and y_0/r_b, respectively. Note that points are omitted for $y_0/r_b = 0$ and 1, see Table 4.1 for their exact values.

plotted alongside the theoretical values in Figure 4.9. The exact value of each point is listed in Table 4.1.

These results indicate that the "experimental" focal length is consistently less than what theoretical calculations predict, though within the expected uncertainty of depth of field. For $y_0/r_b < 0.692$ ($y_0 < 0.45$), the percent error stays below 10%. This indicates that any combination of field effects, including spherical abberation, does not cause the focal length to deviate from Equation 3.19 by more than 10% if the probe is within $y_0/r_b = \pm 0.692$. Since 10% error is considered sufficient for typical plasma experiments, for the purposes of assessing plasma properties with focal length measurements, an electron probe's transverse size ideally should not exceed $w_y = 0.90 \ c/\omega_p$ if centered on axis.

In terms of evaluating what distance to project electrons to, for electrons within

Table 4.1: Focal Length and Error Values from Figure 4.9

y_0/r_b	f_{theory} (c/ω_p)	Depth of Field (%)	f_{QuEP} (c/ω_p)	Percent Error
0	178.	0%	0	100%
0.077	179	0.297%	169	5.24%
0.154	180	1.20%	171	4.99%
0.231	183	2.77%	174	4.99%
0.308	187	5.10%	177	5.24%
0.385	193	8.33%	182	5.54%
0.462	201	12.7%	188	6.16%
0.538	211	18.7%	197	6.92%
0.615	226	26.9%	208	8.03%
0.692	247	38.6%	223	9.61%
0.769	279	56.5%	245	12.2%
0.846	334	87.6%	278	16.8%
0.923	463	160.%	339	26.8%
1	∞	∞	522	–

$y_0/r_b = \pm 0.692$, all electrons will fully "lens" by $x = 37$ mm (223 c/ω_p). Beyond $y_0/r_b = \pm 0.692$, the focal length rapidly starts to increase both theoretically and experimentally.

It is important to note that by using Equation 3.19, we make the approximation that F_y and k are constant, in spite of the fact that the electron is not keeping with the co-moving frame (see Section 3.5.3 and Equation 3.18). For an electron moving at relativistic longitudinal speeds within the fully blown out regime, plasma wakefield theory states that $k \approx 0.5$. Figure 4.10, which plots k as a function of longitudinal position, shows that k is not constant throughout the entire wakefield region. Since experimental electrons are initialized with no longitudinal momenta, the laser pulse will move in z as the electrons move in x, leading to the electrons experiencing different k and F_y at different points in their trajectory as the wakefields move past them. This would inherently affect the measured focal length in both simulation and experiment.

Throughout the center of Region I of the OSIRIS-Quasi3D field maps, k is

approximately constant and is consistent with the theoretical expectations for a relativistic longitudinal electron. The analysis in Figure 4.9 and Table 4.1 confirms that electrons sent in this region (specifically $z = 43.7$), will not have their focal length deviate from theoretical calculations by more than 10%. However, further investigation into how focal length differs from theoretical calculations for different values of z is needed to further quantify how well the thin lens approximation and its associated focal length formulae work for experimental plasma blowout regimes.
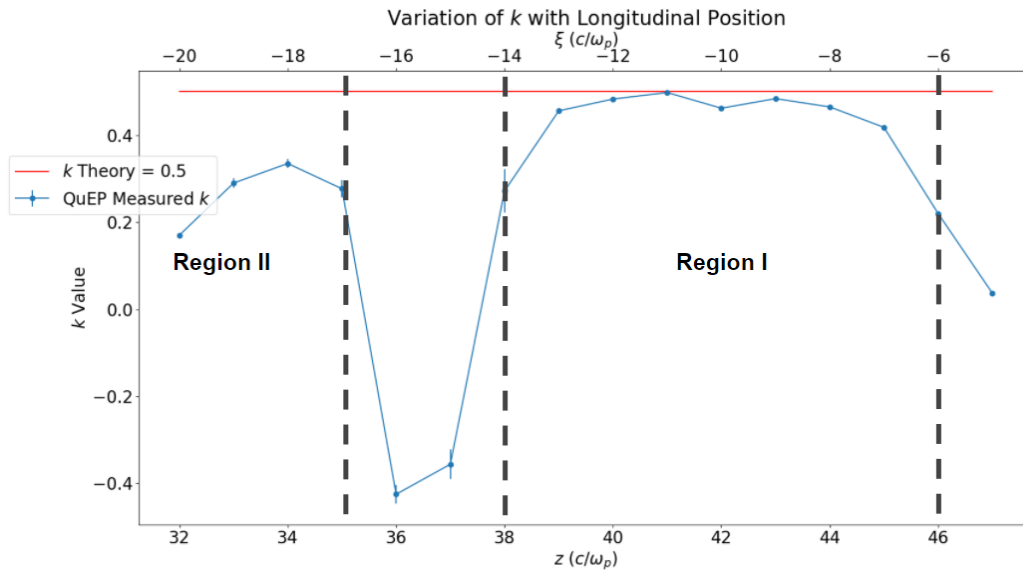

Figure 4.10: Graph of linear focusing field slope k versus longitudinal position. The vertical and horizontal axes correspond to k and longitudinal position (either z or ξ), respectively. Each QuEP measured k value (blue) was found by fitting the linear portion of the M0 electric field, identical to the analysis performed for Figure 3.9. The residuals were used to propagate error, then plotted as error bars. Some points have negligible error, thus their error bars are not visible. k according to PWFA theory is plotted in red. Regions I and II are labeled for comparison with OSIRIS Quasi-3D field maps.

CHAPTER 5

CONCLUSIONS

As the demand for particle accelerators of higher energies grows, and more research is done into their operation, plasma wakefield accelerators are increasingly poised to become the next generation of accelerators. Ongoing research in the field seeks to further understand the field structure of plasma wakes, since wake structure is essential for preserving beam quality. In particular, the Accelerator Test Facility at BNL is conducting a series of experiments which will send a relativistic electron probe transverse to a laser-driven plasma wakefield, then observe the deflected probe profile.

This thesis work was motivated by a need to quickly simulate electron trajectories inside these LWFA in three-dimensional space, so as to account for the cylindrically asymmetric motion of electrons when traveling transverse to a plasma wake. By building upon existing cylindrically symmetric electron tracking codes, the simulation library QuEP was developed. Its tracking accuracy was successfully verified with two analytical calculation tests, and several zero-order predictions of probe trajectories have been made and taken into consideration for future experimental runs at ATF. In the future, QuEP could be further improved by making the behavior of electron probes as a whole more realistic.

Current results produced by QuEP are qualitatively very similar to those produced at ATF, the most key features being the four bright nodes, the masts, and the sail of electrons. In the future, a careful study of smaller electron probes sent through specific areas of the wakefield would indicate which parts of the wakefield correspond to what features.

In terms of the impact of the laser pulse (M1) versus the impact of the induced wakefield (M0), we conclusively determined the induced wakefield dominates the

overall shape of the probe, even resulting in the mast and sail shapes. The laser alone produces modulation features in the plasma whose spacings correspond to the laser wavelength λ and 10λ, depending on how close one is to the driving pulse. The λ modulations are expected, but the origin of the 10λ modulations remain to be studied. For a complete field map (M0+M1), the induced wakefield still maintains the overall shape determined by M0, but is more washed out due to the laser pushing electrons back and forth in z.

Studies of probe height variation and experimental focal length determined that shorter probes provide the most visual clarity in observing nodes and surrounding bubbles in the probe profile. The wider the probe in y, the more the focal length deviates from expected theoretical values, and thus the more "out of sync" those probe features appear in the final profile picture (in terms of how quickly electrons get lensed distance-wise).

In addition to its accuracy in predicting electron trajectories through plasma wakefields, QuEP is open-source. The library is structured so that the electron propagation process occurs independent of electromagnetic field readout. This allows users to easily modify the way electromagnetic field values are calculated or swap out simulation field maps entirely without affecting the integrity of the tracking algorithms. Thus, QuEP has the flexibility to be implemented in any study of electron motion through quasi-static plasma, as long as the field maps are provided.

Overall, this research provides a solid computational reference point for the ongoing transverse electron probe studies of laser-driven plasma wakefields at ATF, and has the potential to be used in many open-ended questions in plasma physics.

BIBLIOGRAPHY

[1] Robert W Hamm and Marianne E Hamm. *Industrial Accelerators and Their Applications*. WORLD SCIENTIFIC, 2012. DOI: `10.1142/7745`. eprint: `https://www.worldscientific.com/doi/pdf/10.1142/7745`. URL: `https://www.worldscientific.com/doi/abs/10.1142/7745`.

[2] M. Koratzinos et al. *TLEP, first step in a long-term vision for HEP*. 2013. arXiv: `1306.5981 [physics.acc-ph]`.

[3] R Assmann et al. "Proton-driven plasma wakefield acceleration: a path to the future of high-energy particle physics". In: *Plasma Physics and Controlled Fusion* 56.8 (2014), p. 084013. DOI: `10.1088/0741-3335/56/8/084013`.

[4] Francis F. Chen. *Introduction to plasma physics and controlled fusion*. Springer, 2018.

[5] E. Esarey, C. B. Schroeder, and W. P. Leemans. "Physics of laser-driven plasma-based electron accelerators". In: *Reviews of Modern Physics* 81.3 (2009), pp. 1229–1285. DOI: `10.1103/revmodphys.81.1229`.

[6] *Laser driven plasma wakefield acceleration*. URL: `http://wp.lancs.ac.uk/spiral/research/laser-driven-plasma-wakefield-acceleration/`.

[7] C. J. Zhang et al. "Capturing relativistic wakefield structures in plasmas using ultrashort high-energy electrons as a probe". In: *Scientific Reports* 6.1 (2016). DOI: `10.1038/srep29485`.

[8] C. E. Clayton et al. "Self-mapping the longitudinal field structure of a nonlinear plasma accelerator cavity". In: *Nature Communications* 7.1 (2016). DOI: `10.1038/ncomms12483`.

[9] Audrey C Farrell. "Simulating beam induced ionization-injection in plasma wakefield accelerators". Undergraduate thesis. Stony Brook University, 2020.

[10] Lubos Brieda. *The Electrostatic Particle in Cell (ES-PIC) Method*. URL: https://www.particleincell.com/2010/es-pic-method. (accessed: 01.16.2021).

[11] Brice Carnahan H.A. Luther James O. Wilkes. *Applied Numerical Methods*. Wiley, 1969.

[12] *OSIRIS*. URL: http://epp.tecnico.ulisboa.pt/osiris. (accessed: 01.17.2021).

[13] W.B. Mori A Davidson A Tableman W An F.S. Tsung W. Lu J Viera R.A Fonseca L.O. Silva. "Implementation of a hybrid particle code with a PIC description in $r-z$ and a gridless description in ϕ into OSIRIS". In: *Journal of Computational Physics* 281 (2015), pp. 1063–1077.

[14] D.A. Edwards and M.J. Syphers. *An Introduction to the Physics of High Energy Accelerators*. Wiley, 1993.

[15] W. Lu et al. "Nonlinear Theory for Relativistic Plasma Wakefields in the Blowout Regime". In: *Physical Review Letters* 96.16 (2006). DOI: 10.1103/physrevlett.96.165002.